APPLIED SCIENCES AND ENGINEERING

Transformation of arginine into zero-dimensional nanomaterial endows the material with antibacterial and osteoinductive activity

Jiaying Li[1]†, Jinjin Ma[1]†, Heng Sun[1]†, Meizhe Yu[2], Huan Wang[1], Qingchen Meng[1], Zexi Li[1], Dachuan Liu[1], Jianzhong Bai[1], Guoping Liu[1], Xiaodong Xing[2]*, Fengxuan Han[1]*, Bin Li[1,3]*

Implant-associated infection is a major threat affecting the success of orthopedic surgeries. Although various materials scavenge bacteria by generating reactive oxygen species (ROS), the intrinsic inability of ROS to distinguish bacteria from cells notably limits the therapeutic effects. Here, we found that the arginine carbon dots (Arg-CDs) that were transformed from arginine exhibited supreme antibacterial and osteoinductive activity. We further designed the Schiff base bond between Arg-CDs and aldehyde hyaluronic acid/gelatin methacryloyl (HG) hydrogel to release Arg-CDs in response to the acidic bone injury microenvironment. The free Arg-CDs could selectively kill bacteria by generating excessive ROS. Furthermore, the Arg-CD–loaded HG composite hydrogel showed excellent osteoinductive activity through inducing the M2 polarization of macrophages by up-regulating interleukin-10 (*Il10*) expression. Together, our findings revealed that transformation of the arginine into zero-dimensional Arg-CDs could endow the material with exceptional antibacterial and osteoinductive activity, favoring the regeneration of infectious bone.

INTRODUCTION

Orthopedic implant–associated infections remain a big clinical challenge that requires extensive surgical interventions (*1*) and long-term antibiotic therapies. *Staphylococcus aureus*, one of the main causes of bone infections, can delay the bone healing process and lead to bone loss (*2*). In addition, the acidic environment of infection is favorable for bacteria to release a variety of factors and form biofilm (*3*). Moreover, because of the overuse of antibiotics, resistant bacteria rapidly emerge (*4*–*6*). To overcome the drug resistance of bacteria, the introduction of antibacterial materials is one of the most promising strategies (*7*–*11*). However, the cytotoxicity of antibacterial agents is a major concern for their clinical application (*12*). Although various efforts have been made to balance antibacterium and biosafety (*13*), reducing the adverse effects and promoting tissue repair during antimicrobial administration remains challenging (*14*).

The main reason why various studies have failed to achieve both antibacterium and tissue regeneration simultaneously is that these materials eliminate bacteria by directly up-regulating reactive oxygen species (ROS) levels (*15*–*17*). However, they are generally toxic to both bacteria and mammalian cells because of the intrinsic inability of ROS to distinguish bacteria from mammalian cells. Moreover, the injured bone microenvironment typically produces excessive ROS that can exacerbate inflammation and delay bone repair (*18*). To date, various attempts to accelerate bone repair by regulating ROS have been made (*19*–*21*). Our previous study has shown that simultaneous elimination of ROS and up-regulation of antioxidant genes, such as Sirtuin1 (*Sirt1*), superoxide dismutase 2 (*Sod2*), and catalase (*Cat*), through manganese dioxide–based composite hydrogels can significantly promote bone regeneration (*22*). Thus, the development of biomaterials that have antibacterial and osteogenic activity simultaneously by ROS regulation may be a promising strategy for infectious bone repair.

Zero-dimensional carbon dots (CDs) exhibit excellent antibacterial activity because of their potential to generate ROS (*23*, *24*). Depending on the surface charge, CDs exhibit completely different effects on bacteria and cells (*24*). Positively charged CDs tend to induce higher endogenous ROS more readily than negatively charged dots, disrupting bacterial membranes. In our previous study, we successfully synthesized positively charged CDs from arginine (Arg), an amino acid residue rich in natural antimicrobial peptides, through a facile pyrolysis process. Because of the moderate positive charge, Arg-CDs efficiently disrupted bacterial membranes while promoting typical mammalian cell growth by modulating ROS levels. Arg-CDs could up-regulate the expression of the intracellular antioxidant enzymes including superoxide dismutase (SOD) and catalase (CAT) in cells, protecting the latter from ROS-induced oxidative damage. On the other hand, the antioxidant enzymes remain almost unchanged in bacteria upon Arg-CD treatment (*25*). Therefore, Arg-CDs may be an ideal candidate for promoting infectious bone repair because of their differential regulating capacity of antioxidant enzymes between cells and bacteria.

In this study, we synthesized Arg-CDs by a simple pyrolysis method. To release Arg-CDs in a well-controlled way in the acidic environment of infectious bone injury, the Arg-CDs were mixed with aldehyde hyaluronic acid (HA-CHO) and gelatin methacryloyl (GelMA, G), which then formed a CD/HA/GelMA composite

[1]Orthopedic Institute, Department of Orthopaedic Surgery, The First Affiliated Hospital, State Key Laboratory of Radiation Medicine and Protection, School of Radiation Medicine and Protection and Interdisciplinary Sciences (RAD-X), Collaborative Innovation Center of Radiation Medicine of Jiangsu Higher Education Institutions, Suzhou Medical College, Soochow University, Suzhou, Jiangsu 215006, China. [2]School of Chemistry and Chemical Engineering, Nanjing University of Science and Technology, Nanjing, Jiangsu 210094, China. [3]School of Biology and Basic Medical Sciences, Suzhou Medical College, Soochow University, Suzhou, Jiangsu 215123, China.
*Corresponding author. Email: binli@suda.edu.cn (B.L.); fxhan@suda.edu.cn (F.H.); xingxiaodong07@njust.edu.cn (X.X.)
†These authors contributed equally to this work.

hydrogel (CHG) as a result of the photocrosslinking of GelMA and Schiff base interaction between Arg-CDs and hydrogel. In addition to the characterizations of the morphology and release behavior of Arg-CDs, the antimicrobial and osteoinductive activity of the composite hydrogel were evaluated in vitro. After implanting composite hydrogel into infectious rat femoral defects, its ability to promote bone formation and eliminate bacteria was assessed in vivo. Last, the underlying mechanism of osteogenesis induced by the composite hydrogel was explored (Fig. 1).

RESULTS

Characterizations of Arg-CDs and the composite hydrogels

Arg-CDs were obtained by a simple pyrolysis method. As shown in Fig. 2A, Arg-CDs were spherical and uniformly dispersed with a diameter of ~7 nm (fig. S1). The ultraviolet-visible (UV-vis) absorption spectra showed notable absorption peaks at the wavelength of 220 and 305 nm, indicating that Arg-CDs were successfully obtained after calcination (Fig. 2B). The osteoinductive activity of Arg and Arg-CDs was measured. The result of alizarin red staining shows that Arg-CDs produced a large amount of calcium deposition, showing higher osteogenic activity. Moreover, with the increase of the concentration, the osteogenic activity of Arg-CDs gradually increased (fig. S2). The antibacterial activity of Arg and Arg-CDs was also performed. The result shows that the number of *S. aureus* colonies in the Arg-CDs group was significantly less than that in Arg. The antibacterial activity of Arg-CDs showed concentration dependency, and Arg-CDs (1 mg/ml) could inhibit about 92% *S. aureus* within 24 hours (fig. S3).

Fourier transform infrared spectroscopy (FTIR) measured whether HA-CHO was successfully obtained. Compared with HA, a new peak was observed at 1731 cm^{-1}, which was ascribed to the C═O stretch of HA-CHO (Fig. 2C). Arg-CDs and HA-CHO were added to the G hydrogel solution to obtain G, HA/GelMA (HG), and CHG composite hydrogels after photocrosslinking. Figure 2D showed the morphology of the composite hydrogels with ordered and uniformly arranged interconnected macropores. However, the interconnected macropores of HG and CHG composite hydrogels collapsed in an acidic solution (pH 5.5), indicating that the structure of our fabricated HG and CHG composite hydrogels

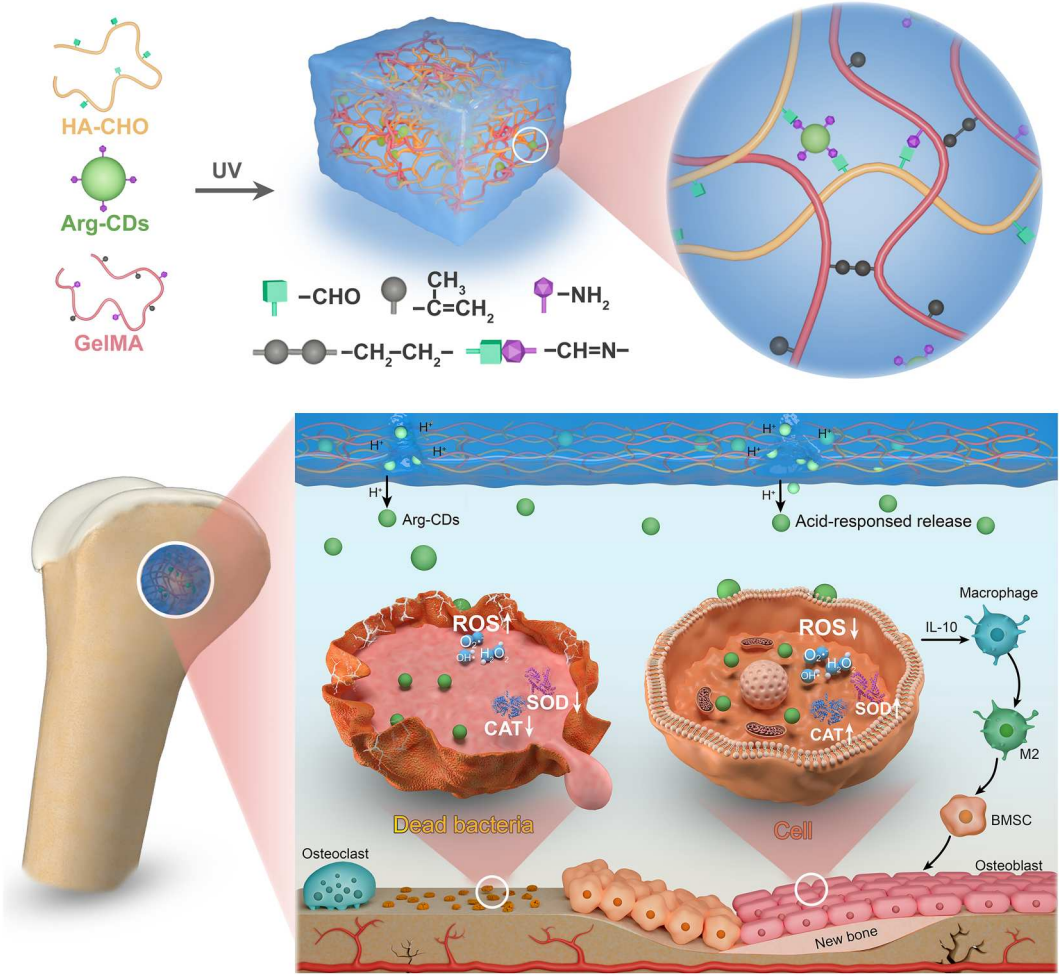

Fig. 1. Schematic illustration of bacterial elimination and osteogenic enhancement by the CHG composite hydrogel. The hydrogel releases Arg-CDs in response to the acidic bone injury microenvironment, which selectively kills bacteria by producing excessive ROS. Meanwhile, it reduces the intracellular ROS level by up-regulating antioxidase expression and promotes cell proliferation. Moreover, it exhibits superior osteoinductive properties owing to the promotion of M2 polarization of macrophages by up-regulating *Il10* expression. UV, ultraviolet; IL-10, interleukin-10; BMSC, bone marrow mesenchymal stem cell.

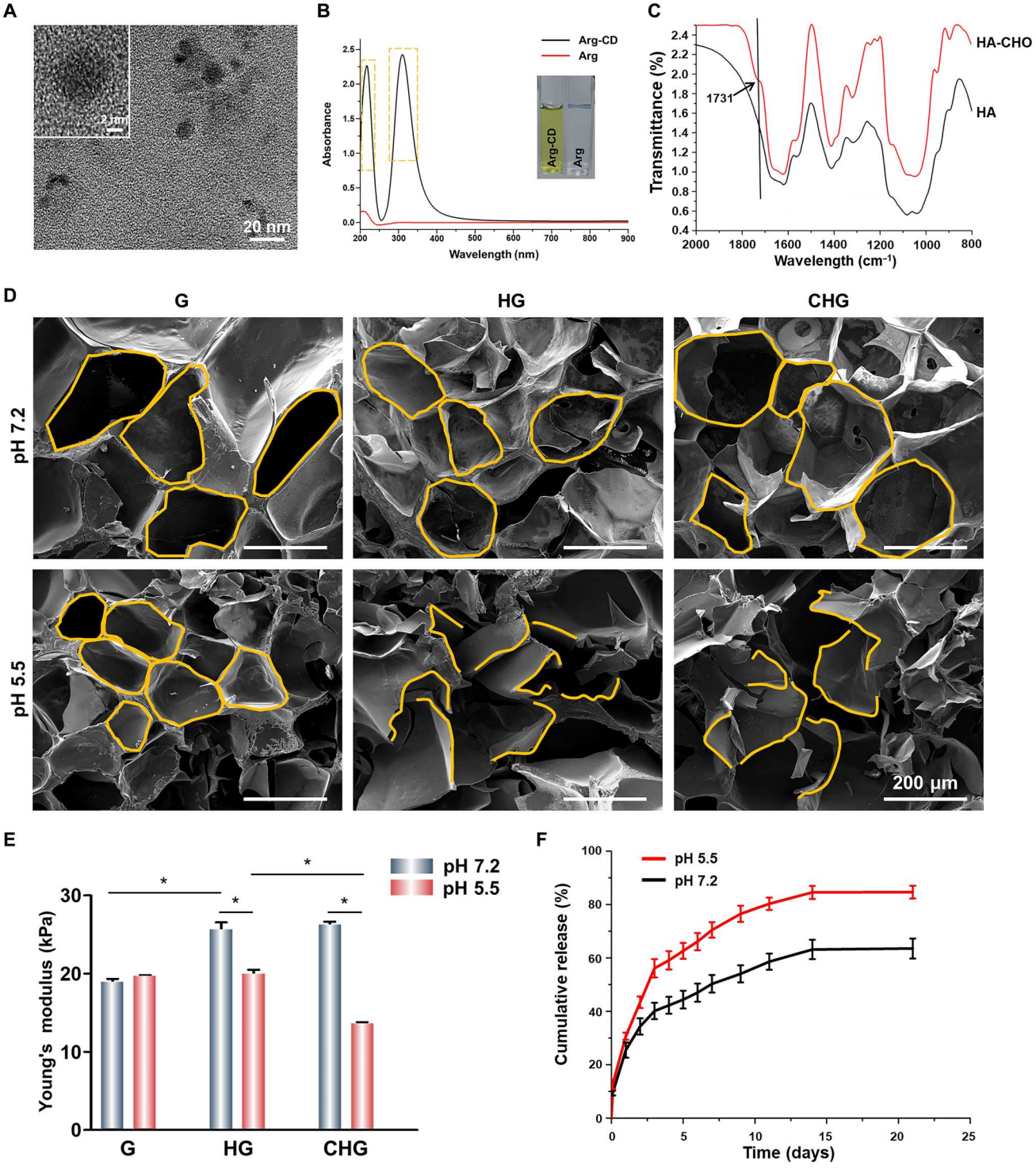

Fig. 2. Characterizations of Arg-CDs and composite hydrogels. (**A**) Transmission electron microscopy images of Arg-CDs. (**B**) UV-visible (UV-vis) absorption spectra of Arg-CDs. (**C**) Fourier transform infrared spectroscopy spectra of HA and HA-CHO. (**D**) Scanning electron microscopy (SEM) images of the composite hydrogels treated by a neutral and acidic solution, respectively. (**E**) Compressive strength of the composite hydrogels. (**F**) Release curve of Arg-CDs from the composite hydrogels under neutral and acidic solution, respectively. (*$P < 0.05$).

was disrupted in response to acidic condition. Furthermore, the compressive strength of hydrogels increased from 18.8 ± 0.7 kPa for the G hydrogel alone to 25.6 ± 1.3 and 26.3 ± 0.5 kPa for the HG and CHG composite hydrogels, respectively. While C═N bonds ruptured in response to the acidic microenvironment, the structure of the HG and CHG composite hydrogels was fragmentized, accompanied by a decrease in compressive strength of HG from 25.6 ± 1.3 to 20.0 ± 0.7 kPa, as well as CHG from 26.3 ± 0.5 to 13.6 ± 0.3 kPa (Fig. 2E).

The Arg-CD release characteristics of the CHG composite hydrogel were investigated. To simulate the acidic microenvironment of injured bone, Arg-CDs release tests were performed by measuring the UV-vis absorption spectra at a wavelength of 305 nm in pH 5.5 and pH 7.2 buffer solutions, respectively. As shown in Fig. 2F, in acidic media, the CHG composite hydrogel released 84.7 ± 2.4% of Arg-CDs within 21 days, which was significantly more than that in neutral media (63.5 ± 2.7%). This behavior was attributed to the acid-responsive cleavage of C═N groups formed between Arg-CDs and hydrogel.

Cell morphology and viability on the composite hydrogels

To evaluate the biocompatibility of composite hydrogels, rat bone marrow mesenchymal stem cells (BMSCs) were seeded on tissue culture plates (Ctrl group) and composite hydrogels. The cytoskeleton staining shows that BMSCs adhered and spread efficiently on G, HG, and CHG composite hydrogels, exhibiting good biocompatibility (Fig. 3A). The morphological images of cells show that BMSCs spread on composite hydrogels (Fig. 3B), demonstrating that the addition of Arg-CDs did not affect the biocompatibility of composite hydrogels. The cell counting kit-8 (CCK-8) assay of composite hydrogels shows that the number of cells in all groups increased within 5 days. Encouragingly, the CHG composite hydrogel significantly promoted cell proliferation compared to the other groups (Fig. 3C), which was consistent with our previously reported results (*25*).

In vitro antibacterial effects of the composite hydrogels

S. aureus, the main cause of orthopedic implant–associated infection, was used to measure the antibacterial activity of composite hydrogels. Results of acridine orange/ethidium bromide (AO/EB) staining show that the number of dead bacteria on the CHG composite hydrogel was notably increased (Fig. 4A). Furthermore, the inhibition zone experiment shows that the distance without bacterial colonies of CHG composite hydrogel reached about 2 mm, which was considerably longer than that of G and HG composite hydrogels (Fig. 4B). The results of the standard plate counting assay show that the number of *S. aureus* colonies on the CHG composite hydrogel was about 14%, while those on G and HG composite hydrogels was about 100 and 93%, respectively (Fig. 4C and fig. S4A). As shown in Fig. 4D, the bacterial membranes on G and HG composite hydrogels were intact and smooth, and the number of bacterial colonies was much larger on G and HG composite hydrogels. In turn, the structural integrity of bacteria on the CHG composite hydrogel was obviously impaired, inducing leakage of bacterial cytoplasm and reduction in bacterial numbers. Moreover, the antibacterial kinetics of composite hydrogels was studied by *S. aureus*. As shown in Fig. 4E, the CHG composite hydrogel rapidly eradicated living bacteria, and the bacterial killing activity was time dependent. The CHG composite hydrogel inactivated 88% of *S. aureus* within 24 hours (fig. S4B).

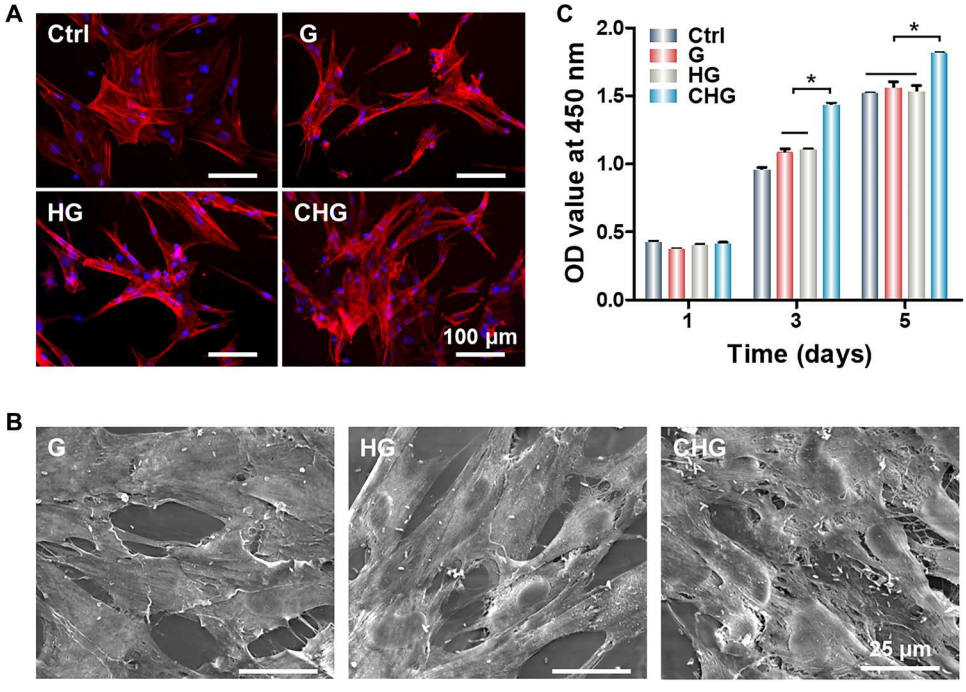

Fig. 3. Cell morphology and proliferation on the surface of composite hydrogels. (**A**) Cytoskeleton staining of BMSCs seeded on the surface of composite hydrogels. (**B**) SEM images of cell morphology on the surface of composite hydrogels. (**C**) CCK-8 cell proliferation assay. (*$P < 0.05$). OD, optical density.

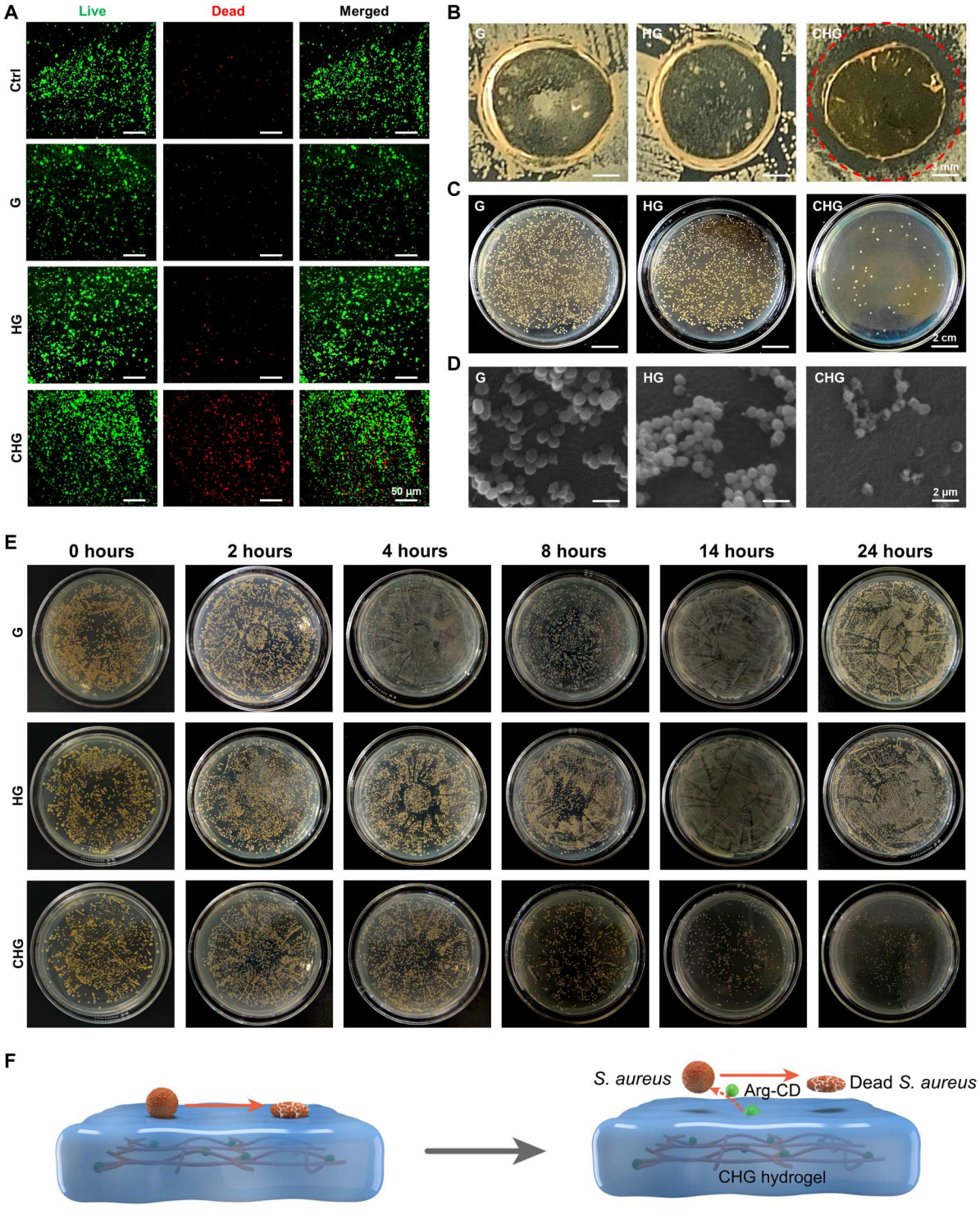

Fig. 4. Antibacterial properties of the composite hydrogels. (**A**) AO/EB staining images of *S. aureus* cultured on the composite hydrogels. (**B**) Inhibition zones of the composite hydrogels' contact with *S. aureus*. (**C**) Colonies of *S. aureus* counted on the composite hydrogels. (**D**) Morphology of *S. aureus* cultured on the surface of composite hydrogels. (**E**) Colonies of *S. aureus* counted on composite hydrogels at different time points. (**F**) Illustration of the states of bacteria on the composite hydrogels: CHG composite hydrogel eliminates *S. aureus* on and around its surface.

Competitive colonization of bacteria and cells on the composite hydrogels

Successful colonization of cells on the implant surface favors osteogenesis, while bacterial colonization may induce infection. To examine the competitive colonization of cells and bacteria, BMSCs and *S. aureus* were simultaneously seeded on the surface of composite hydrogels (Fig. 5C). Scanning electron microscopy (SEM) images indicate that the CHG composite hydrogel promoted cell adhesion and spread, and there is a very small number of bacteria on its surface (Fig. 5A). Moreover, bacteria can internalize and survive well within cells, which may be the reason behind chronic infection and recurrence of infection. Therefore, in the present study, we labeled BMSCs and *S. aureus* with DiO perchlorate (green) and DiD perchlorate (red), respectively. Subsequently, DiO-labeled BMSCs and DiD-labeled *S. aureus* were simultaneously seeded on the hydrogel surface. After 24 hours, the extracellular bacteria were eliminated by gentamicin (60 μg ml^{-1}). As shown in Fig. 5B, the amount of *S. aureus* inside cells was significantly higher on G and HG composite hydrogels compared with CHG composite hydrogels, showing that bacteria grew well on the surface of G and HG composite hydrogels and even internalized and survived within BMSCs. In contrast, the CHG composite hydrogel significantly maintained the viability of BMSCs, while most bacteria on it were moribund and underwent apoptosis, indicating that CHG composite hydrogels may be a good antibacterial and cell survival–promoting candidate scaffold.

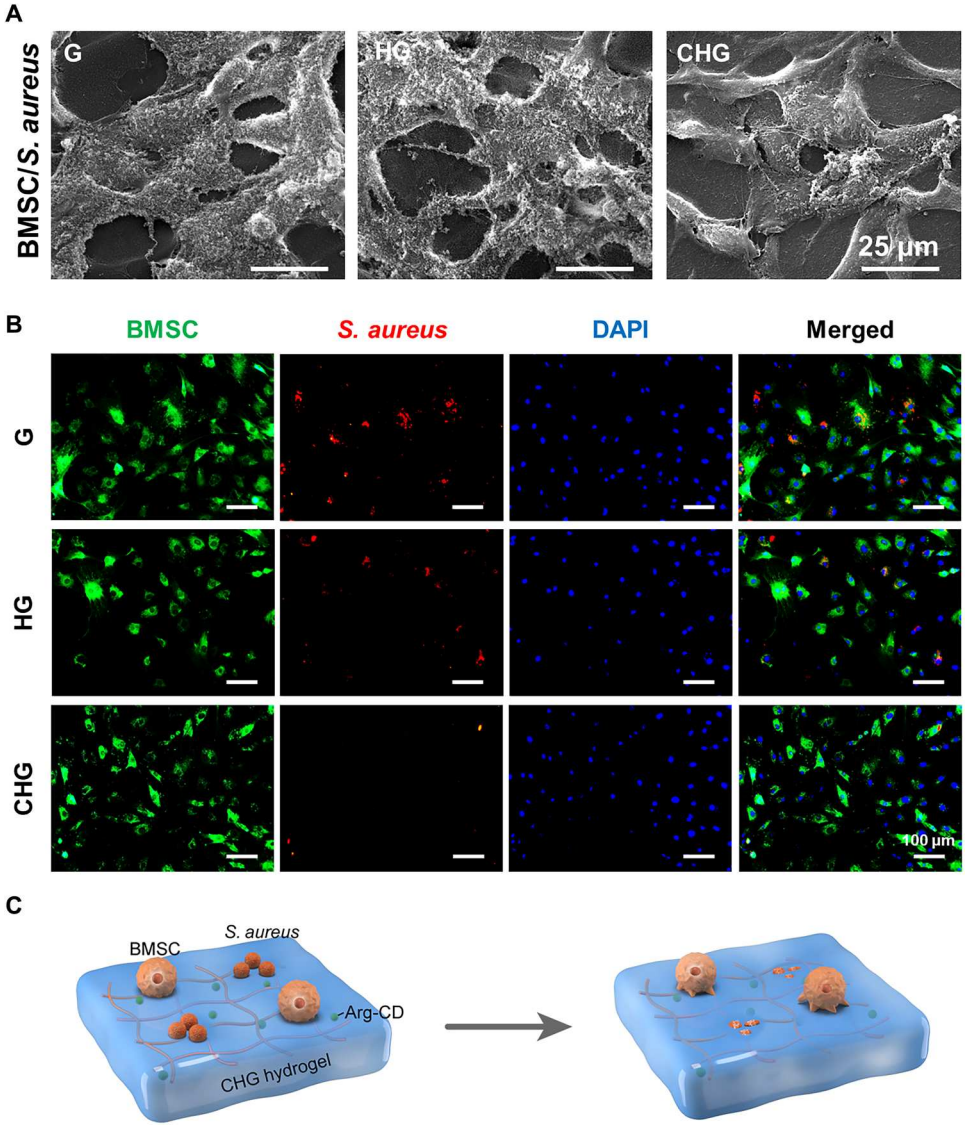

Fig. 5. Competitive colonization assay of cells and bacteria on the surface of composite hydrogels. (**A**) Morphology of BMSCs and *S. aureus* cultured on the surface of composite hydrogels. (**B**) Images of intracellular bacteria inside the cells, which adhere to the scaffold surface. Green indicates the DiO labeling of BMSCs, red indicates DiD labeling of *S. aureus*, and blue depicts the 4′,6-diamidino-2-phenylindole (DAPI) staining of the nucleus. (**C**) Illustration of the cell and bacteria coculture system on the composite hydrogels: CHG composite hydrogel selectively eliminates *S. aureus* and promotes cell adhesion and growth.

ROS regulation by the composite hydrogels in bacteria and cells

To explore the mechanism of killing bacteria and maintaining cell survival of the CHG composite hydrogel, *S. aureus* and BMSCs were treated with composite hydrogels, and the ROS levels in *S. aureus* and BMSCs were quantified. Compared with G and HG composite hydrogels, the intracellular ROS levels in *S. aureus* and BMSCs significantly increased upon exposure to the CHG composite hydrogel (Fig. 6A). However, antioxidant properties of the CHG composite hydrogel in bacteria and cells were completely distinct. Total antioxidant enzyme, including CAT (the enzyme that can catalyze the decomposition of hydrogen peroxide into oxygen and water) and SOD (an important member of the antioxidant enzyme system in biological system), activities of *S. aureus* cultured on the CHG composite hydrogel were effectively inhibited. Thus, *S. aureus* was unable to eliminate excessive intracellular ROS and was more vulnerable to oxidant-induced damage. However, unlike *S. aureus*, the CHG composite hydrogel showed no evident inhibiting effect on the antioxidant enzymes in BMSCs, while enhancing cellular CAT and SOD activities (Fig. 6, B and C). Therefore, the

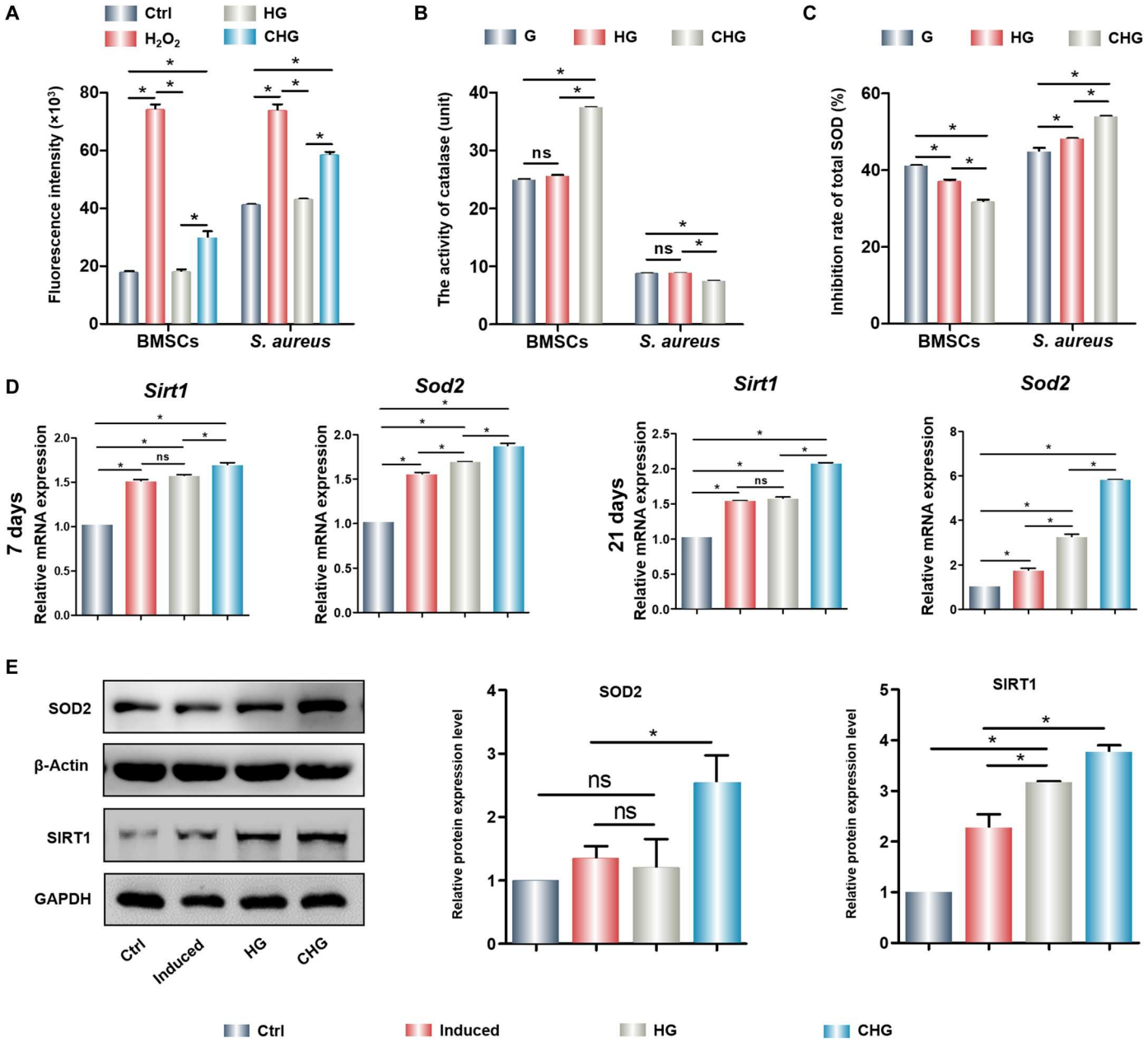

Fig. 6. ROS generation and antioxidant effects of cells and bacteria on the composite hydrogels. (**A**) Quantity of ROS generated in cells and bacteria cultured on composite hydrogels. (**B**) CAT activity of BMSCs and *S. aureus* cultured on the composite hydrogels. (**C**) SOD inhibition rate of BMSCs and *S. aureus* cultured on the composite hydrogels. (**D**) Expression of antioxidant genes of BMSCs cultured on the composite hydrogels. (**E**) Expression and quantification of antioxidant protein of BMSCs cultured on the composite hydrogels. (*$P < 0.05$). ns, not significant; GAPDH, glyceraldehyde-3-phosphate dehydrogenase.

suppression of total CAT and SOD activities was obviously different in bacteria and cells, resulting in notably superior ROS levels in bacteria than that in cells. The results of 2,7-Dichlorodi-hydrofluorescein diacetate (DCFH-DA) staining consistently show that the CHG composite hydrogel significantly scavenged cellular ROS (fig. S5). The antioxidant property of Arg-CDs alone was detected; the results were demonstrated that Arg-CDs could significantly up-regulate the expression of antioxidant genes, such as *Sirt1* and *Sod2* (fig. S6). After developing composite hydrogel, we also found that the CHG composite hydrogel promoted the gene expression of *Sirt1* and *Sod2* and protein of SIRT1 and SOD in BMSCs (Fig. 6, D and E), indicating that it could resist oxidative damage by up-regulating antioxidant genes and proteins. In conclusion, the CHG composite hydrogel is an excellent candidate for eliminating bacteria and promoting cell proliferation.

In vitro osteogenic effect of cells cultured on the composite hydrogels

The osteogenic properties of Arg-CDs alone were performed by alkaline phosphatase (ALP) and alizarin red staining, as well as the detection of osteogenic gene expression. The results indicate the excellent osteoinductive activity of Arg-CDs (fig. S7). To detect the osteoinductive activity of composite hydrogels in vitro, BMSCs were treated with composite hydrogels and cultured for 7 and 21 days, respectively. ALP staining indicates that the CHG composite hydrogel significantly up-regulated the expression of ALP (Fig. 7A). After 21 days, a large number of calcium nodules were observed in the CHG group. In contrast, a fewer calcium deposition was produced in HG and G groups (Fig. 7B). Polymerase chain reaction (PCR) results show that the CHG composite hydrogel significantly promoted the expression of osteogenesis-related genes, such as secreted phosphoprotein 1 (*Spp1*), alkaline phosphatase (*Alpl*), runt-related transcription factor 2 (*Runx2*), type I collagen (*Col1a1*), and bone gamma-carboxyglutamate protein (*Bglap*) (Fig. 7C). Likewise, Western blot results indicate that the CHG composite hydrogel markedly promoted osteogenic protein expression, including RUNX2, OPN, COL1, and OCN, demonstrating that the CHG composite hydrogel effectively induced osteogenic differentiation of BMSCs (Fig. 7, D and E).

Promotion of in vivo bone formation by the composite hydrogels

The composite hydrogels were implanted subcutaneously to observe ectopic bone formation (fig. S8A). After 4 weeks, HG and CHG composite hydrogels were characterized. The results of alizarin red staining show that CHG composite hydrogels produced more calcium deposits than that of HG composite hydrogels (fig. S8C), but there were no calcium deposits in HG and CHG composite hydrogel before subcutaneous implantation (fig. S8B). The results of hematoxylin and eosin (H&E) staining exhibit that more new bone was generated in the CHG composite hydrogels than HG hydrogels, demonstrating that CHG composite hydrogels have osteoinductivity (fig. S8D).

Composite hydrogels were implanted into the rat femoral defects to observe bone formation. In the *S. aureus* group, almost no bone formation was observed at 4 weeks after surgery. Partial bone tissue was found in the femoral defects of the HG + *S. aureus* group, and there was observable new bone formation in the CHG + *S. aureus* group (Fig. 8A). The percent bone volume (BV/TV) in the CHG + *S. aureus* group reached about 28% in the fourth week postsurgery. Moreover, the values of the thickness and number of trabecular thickness (Tb.Th and Tb.N) in the CHG + *S. aureus* group were significantly higher than that in the HG + *S. aureus* and *S. aureus* groups, while trabecular separation (Tb.Sp) was the lowest. After 8 weeks, the results of bone formation also show that the CHG + *S. aureus* group significantly promoted bone regeneration with a BV/TV value larger than 39% (Fig. 8B). H&E staining and Masson staining likewise suggest that the CHG composite hydrogel could promote bone formation and bone maturation (Fig. 8, C and D).

In vivo antibacterial effects of the composite hydrogels

Giemsa staining was executed to evaluate the bacteria killing effect of composite hydrogels in vivo. Four weeks after implantation, a large number of *S. aureus* were observed at the sites of the femoral defect in the groups of *S. aureus* and HG + *S. aureus* composite hydrogel. However, CHG composite hydrogels eliminated almost all *S. aureus*, and femoral defects were filled with new bone without any infection. Furthermore, the number of *S. aureus* in femoral defects treated by *S. aureus* and the HG + *S. aureus* composite hydrogel was significantly more than that in the CHG + *S. aureus* group at 8 weeks after implantation (fig. S9A). The viable bacteria at the sites of bone defect were also counted. The results suggest that there were about 245.5 CFU/mm^2 of *S. aureus* on the surface of the new bone in the HG composite hydrogel group, while only 8.6 CFU/mm^2 of *S. aureus* in the CHG composite hydrogel group at 4 weeks after surgery. After 8 weeks, the viable *S. aureus* on the surface of the new bone in the HG composite hydrogel group was not increased (about 252.2 CFU/mm^2) compared to that at 4 weeks after surgery, indicating that the bacteria were not proliferating. However, there were only 10.7 CFU/mm^2 of *S. aureus* in the CHG composite hydrogel group at 8 weeks after surgery, which was much lower than that in the HG composite hydrogel, demonstrating that the CHG composite hydrogel significantly eliminated bacteria and promoted bone regeneration (fig. S9B).

Osteogenic mechanism of the composite hydrogels

To further explore the regulatory effect and potential mechanism of the CHG composite hydrogel on BMSCs, RNA sequencing was performed. Principal components analysis indicates that the control group (Ctrl) exhibited a distinct transcriptome profile compared to the HG and CHG groups, with a significant distance on the principal component 1 (PC1) (Fig. 9A). This implies that composite hydrogels markedly influenced the cells on them. Moreover, HG and CHG composite hydrogels were separated on PC2, demonstrating that Arg-CDs further regulated the seeded BMSCs. The gene expression heatmap also showed differential gene expressions between HG and CHG groups (Fig. 9B). To reveal the functions of highly expressed genes in the CHG group, gene ontology (GO) analysis was performed. The results displayed several GO terms related to immunomodulation, including "positive regulation of cytokine production," "lymphocyte activation," "inflammatory response," etc. (Fig. 9C). This implies that Arg-CDs may improve tissue regeneration through immunomodulation. Consistently, gene set enrichment analysis (GSEA) indicated obvious enrichment of genes in the "innate immune response activating signal transduction" and "lipopolysaccharide-mediated signaling pathway," further

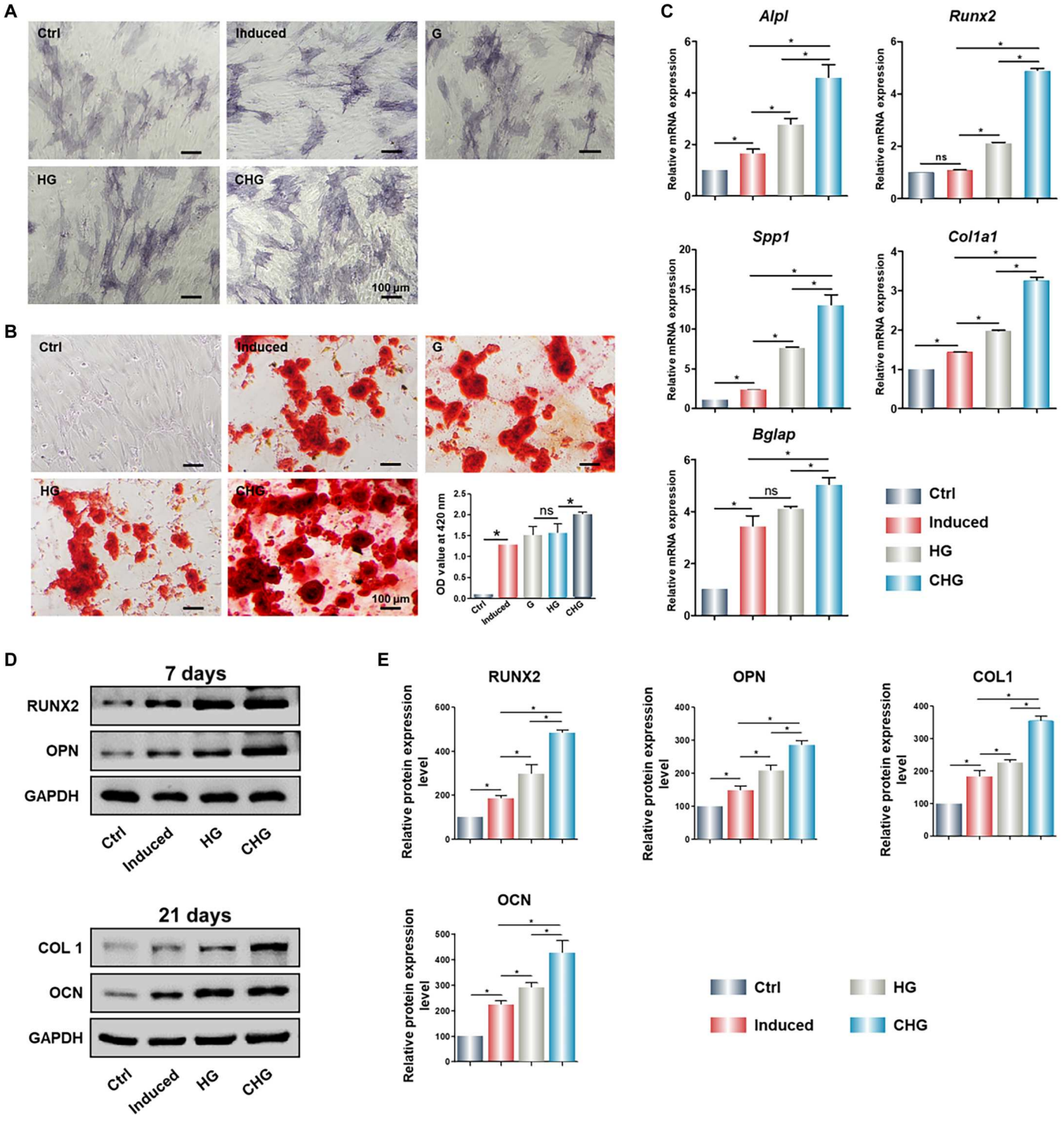

Fig. 7. In vitro osteogenesis of BMSCs cultured on the composite hydrogels. (**A**) ALP staining of BMSCs seeded on the composite hydrogels. (**B**) Alizarin red staining of BMSCs seeded on the composite hydrogels. Expression of osteogenesis-related (**C**) genes and (**D**) proteins of BMSCs cultured on the composite hydrogels. (**E**) Quantification of osteogenesis-related proteins of BMSCs cultured on the composite hydrogels. (*$P < 0.05$).

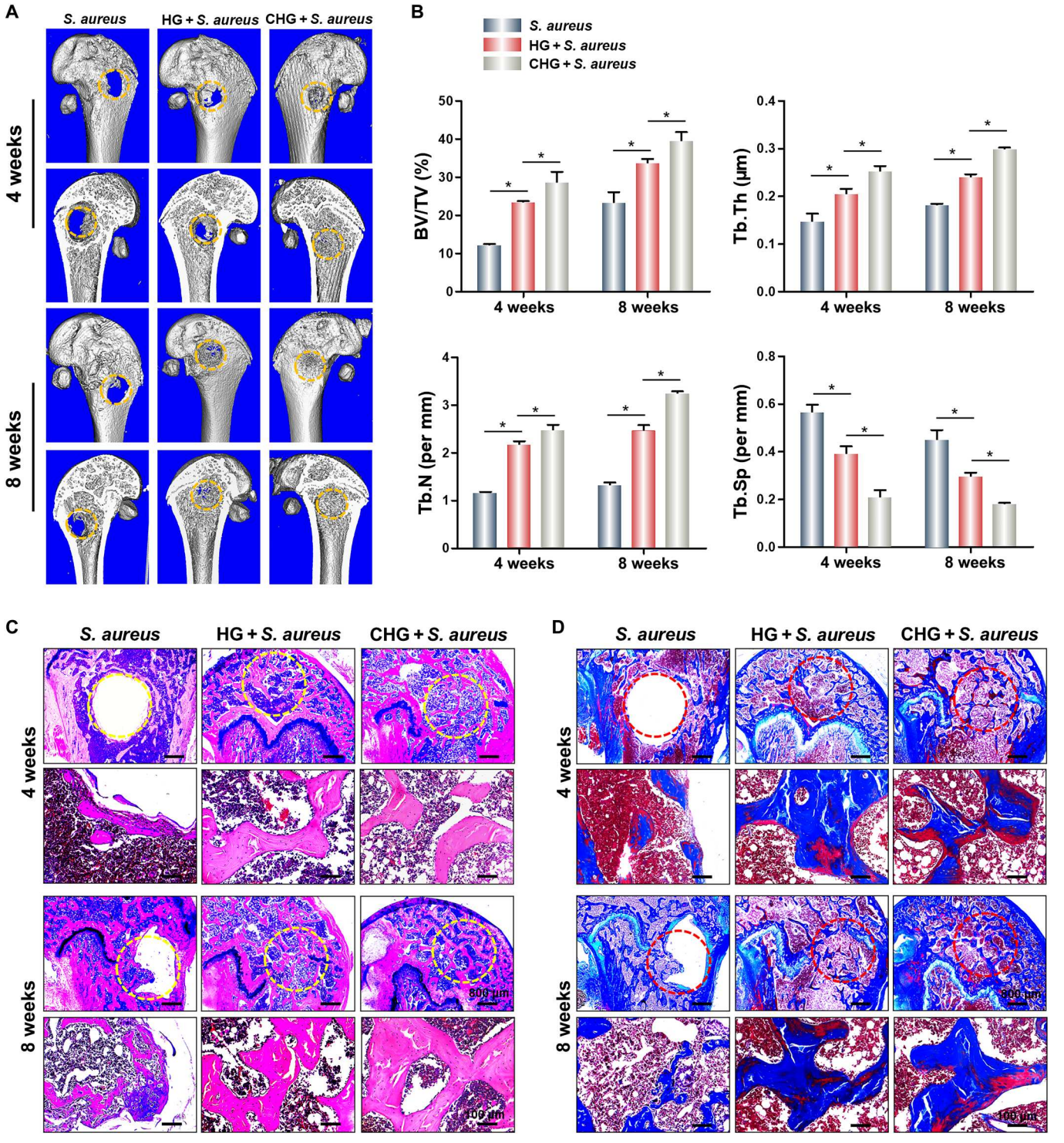

Fig. 8. Promotion of bone formation by the composite hydrogels. (**A**) Micro–computed tomography of harvested femurs. (**B**) Quantitative analysis of newly regenerated bone tissues. (**C**) H&E staining of femoral critical-sized defects in rats. (**D**) Masson staining of femoral critical-sized defects in rats. ($n = 3$; *$P < 0.05$).

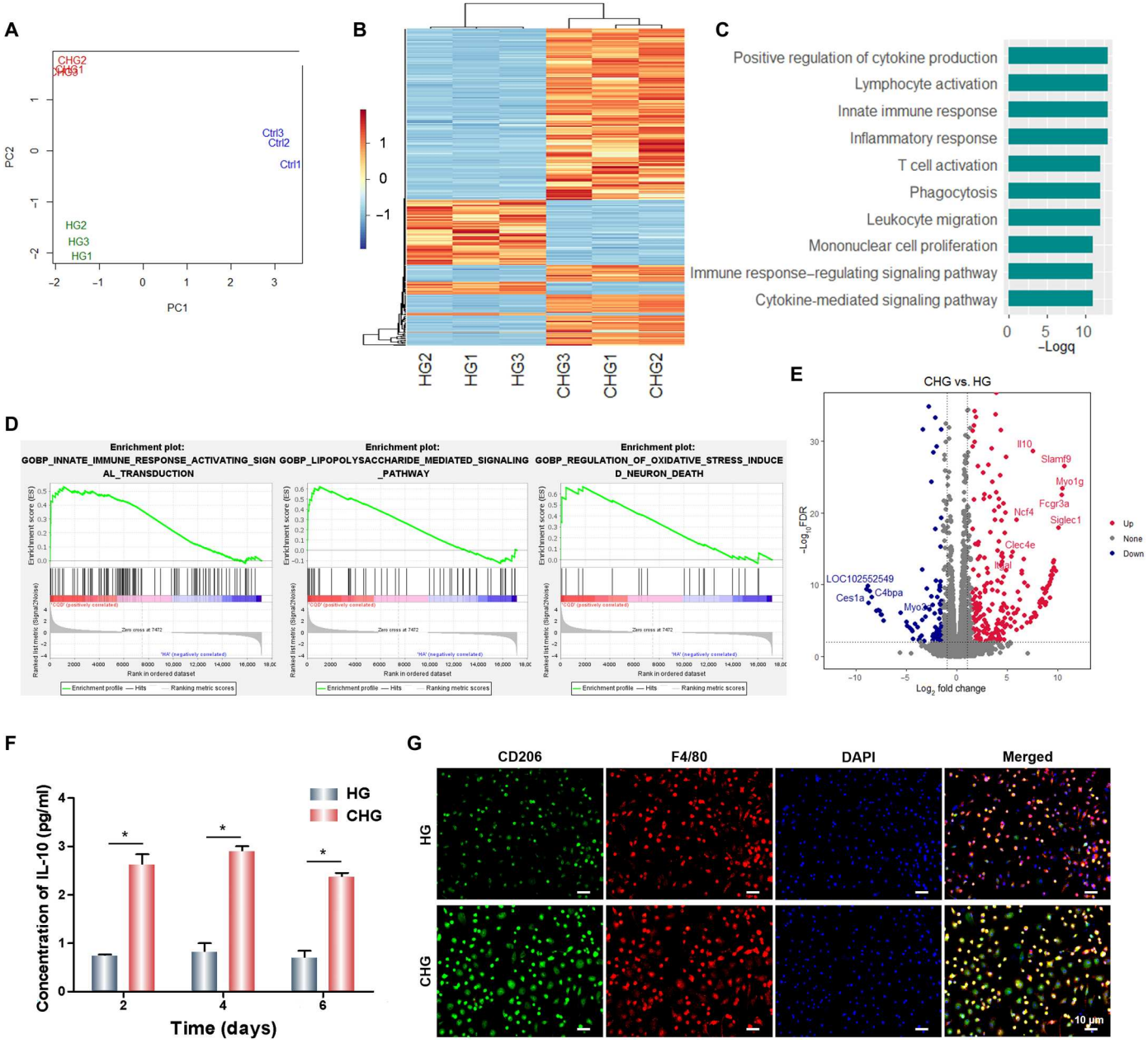

Fig. 9. Exploration of the osteogenic mechanism of the composite hydrogels. (**A**) Principle components analysis. (**B**) Gene expression heatmap. (**C**) Gene ontology analysis. (**D**) Gene set enrichment analysis. (**E**) Volcano plot showing differentially expressed genes between CHG and HG groups. (**F**) Detection of *Il10* released from BMSCs. (**G**) CD206 and F4/80 immunofluorescence of BMMs. (*$P < 0.05$).

confirming the role of Arg-CDs in the immune response (Fig. 9D). Note that the CHG composite hydrogel also up-regulated genes associated with oxidative stress, implying that it may regulate the cellular response to ROS more directly.

We further identified interleukin-10 (*Il10*) as one of the top up-regulated genes in the CHG group (Fig. 9E). The results show that the CHG composite hydrogel significantly promoted the secretion of *Il10* from BMSCs, and the concentration of *Il10* secreted by BMSCs cultured on CHG samples was two to three times higher than that on the HG composite hydrogel (Fig. 9F). Moreover, bone marrow mononuclear cells (BMMs) were seeded on the surface of composite hydrogels and cultured with media that had been used for BMSC culture on composite hydrogels. We found that the conditioned media from the BMSC cultured on the CHG composite hydrogel significantly up-regulated the expression of CD206 in BMMs, while the expression of CD206 was lower in BMMs cultured with conditioned media from BMSCs cultured on the HG composite hydrogel, indicating that the CHG composite hydrogel significantly induced M2 macrophage polarization (Fig. 9G). The results of immunofluorescence also show that the CHG composite hydrogel could promote the expression of CD206 at the infection sites, indicating that CHG composite hydrogels induced M2

macrophage polarization and provided excellent immune microenvironment for infectious bone defect repair (fig. S10). Furthermore, the CHG composite hydrogel also promoted the secretion of IL-10 from BMMs, which was much higher than that from BMSCs (fig. S11). To explore the correlation between BMSCs and immune cells in the process of osteogenic differentiation of BMSCs, we cultured BMSCs with two different culture media. The one is the extract liquid of CHG composite hydrogel, the other one is the BMM conditioned culture media. To confirm that BMMs were an M2 phenotype, BMMs were seeded on the surface of composite hydrogels; the expression of CD206 in BMMs cultured with CHG composite hydrogels was higher than that of HG, indicating that CHG composite hydrogels induced M2 macrophage polarization (fig. S12). Both above media are from osteogenic induction media. After 14 days, alizarin red staining was performed. The result suggests that the conditioned media that have cultured BMMs notably promoted osteogenic differentiation of BMSCs compared to the extract liquid of CHG composite hydrogel, producing a large amount of deposit (fig. S13). Together, the M2 macrophage may accelerate osteogenesis in an *Il10*-dependent manner. To further demonstrate that CHG promoted the osteogenic differentiation of BMSCs by up-regulating *Il10*, we measured the osteogenic activity of BMSCs after silencing the expression of *Il10*. The results indicate that CHG significantly promoted the expression of the osteogenesis-related proteins such as RUNX2 and OCN. However, after silencing the gene expression of *Il10*, the osteogenic activity of BMSCs decreased sharply, and the CHG composite hydrogel also showed negligible capacity for the promotion of osteogenic differentiation of BMSCs (fig. S14). Therefore, we can conclude that CHG promoted the osteogenic differentiation of BMSCs by up-regulating *Il10*.

DISCUSSION

Currently, orthopedic implant–associated infections are typical complications affecting the process of bone healing (*26*). ROS is a double-edged sword. Excessive ROS produced by antibacterial agent can effectively inhibit bacterial growth, but acting by producing ROS in situ immensely limits the osteogenic effects of antibacterial agent and increases oxidative stress damage for the surrounding healthy tissue (*20*). Therefore, balancing antibacterial activity and osteogenesis is the key to achieving infectious bone repair.

After transforming Arg into zero-dimensional carbon-based material, i.e., Arg-CDs, abundant ROS could be produced because of the high level of surface charge. In this study, we successfully prepared the Arg-CD–based CHG composite hydrogel that sustained released Arg-CDs in response to the acidic microenvironment of bone injury, demonstrating that the C═N groups in the CHG composite hydrogel were cleaved in an acidic environment. The acidic environment at the infection site can promote bacteria to release a variety of factors and form biofilm (*3*). In this study, the released Arg-CDs up-regulate ROS levels in bacteria and exhibit excellent antibacterial activity, which is consistent with the findings in previous studies that excessive ROS can disrupt bacterial proteins, lipids, metabolites, and the bacterial membrane (*27*, *28*). Unexpectedly, Arg-CDs significantly scavenge intracellular ROS by up-regulating the expression of antioxidase (SOD and CAT) and antioxidant genes (*Sirt1* and *Sod2*), as well as proteins (SIRT1 and SOD2). Several studies suggest that guanidinium-functionalized materials can penetrate bacteria cell membrane and effectively kill bacteria (*29*–*31*). Arg is an amino acid that only carries a guanidine group, exhibiting excellent antibacterial activity (*32*). Unexpectedly, we found that the antibacterial activity of Arg-CDs was higher than Arg, which may be contributed to the higher positive charge. The surface charges of resultant Arg-CDs are moderately positive with values at neutral pH. As the bacterial membrane surface is more negatively charged than mammalian cells, Arg-CDs exhibit different affinity to bacterial and mammalian cells via electrostatic interaction. Therefore, Arg-CDs preferentially interact with bacteria over cells, allowing Arg-CDs to disrupt bacterial membrane and kill microorganisms. Moreover, in bacteria, the expression of antioxidase (SOD and CAT) was inhibited, the bacteria cannot eliminate the generated ROS, and the bacterial membranes were disrupted. A study reported that CDs obtained from spermidine (CD_{Spds}) showed obvious antibacterial activity. Compared to spermidine alone, CD_{Spds} shows smaller size and higher positive charge; thus, the minimal inhibitory concentration of CD_{Spds} is lower and can efficiently kill bacteria (*33*). Therefore, the transformation of the Arg molecules into zero-dimensional nanomaterial could endow the material with exceptional antibacterial activity.

For orthopedic implant–associated infection, the damaged bone microenvironment typically produces excessive ROS that can exacerbate inflammation and delay bone repair (*14*). Various attempts have been made to accelerate bone repair by modulating ROS (*15*–*17*). Our previous study showed that simultaneous elimination of ROS and up-regulation of antioxidant genes through manganese dioxide–based composite hydrogels significantly promotes bone regeneration (*18*). In this study, Arg-CD showed excellent antibacterial activity compared to Arg, and it could significantly kill bacteria via the up-regulation of ROS in bacteria. In addition, the Arg-CD produced large amounts of calcium deposits and exhibited higher osteoinductive activity than Arg. Moreover, Arg-CDs released from engineered CHG composite hydrogel in response to the acidic bone injury microenvironment also showed excellent osteogenesis both in vitro and in vivo. Various studies have demonstrated that up-regulation of antioxidase and antioxidant genes and proteins can reduce oxidative damage and promote osteogenesis (*22*, *34*, *35*). Here, the obtained CHG composite hydrogel exhibited excellent antioxidant property and osteogenic activity. To further elucidate the underlying mechanism by Arg-CD–triggered osteogenic induction, we investigated the gene expression profile of CHG composite hydrogel–treated BMSCs by RNA sequencing. The sequencing data reveal that the expression of *Il10* in BMSCs was markedly up-regulated in the CHG composite hydrogel–treated group compared with Ctrl and HG. Various studies have demonstrated that a material that can enhance the activities of SOD and CAT may also up-regulate the level of *Il10*, synergistically inhibiting the inflammatory responses (*36*–*39*). Therefore, the activation of *Il10* gene expression by Arg-CDs may be resulted from its excellent antioxidant performance. We also attempted to reveal the underlying mechanism of *Il10* up-regulation by the material. Kyoto Encyclopedia of Genes and Genomes signaling pathway enrichment analysis showed that Toll-like receptor (TLR) and Janus kinase–signal transducer and activator of transcription (JAK-STAT) signaling pathways were activated in the CHG group (fig. S15A). As TLR and JAK-STAT are the pathways regulating c-Maf (*40*, *41*), which, in return, up-regulates *Il10* (*42*), we speculate that CHG improves osteogenesis, at least

partially, by TLR, JAK-STAT pathways, and c-Maf. In line with this, Xu *et al.* (*42*) found that c-Maf directs IL-10 regulation during Th17 polarization, and our sequencing data also demonstrated that CHG composite hydrogel significantly promoted the expression of *Mafb* and *Maf* compared to HG (fig. S15B). *Spp1* and *Ccr1*, the target genes of c-Maf, were also up-regulated by CHG composite hydrogel (fig. S15B) (*43*–*45*). It has been reported that *Mafb* and *c-Maf*, a part of the large *Maf* transcription factor family, can bind to DNA through the basic leucine zipper motif (*46*). *Mafb* and *c-Maf* function alone or together to control cell fate and differentiation in bone, epithelial cells, lens, macrophages, and pancreas (*47*–*49*). Therefore, it is possible that CHG composite hydrogel up-regulates IL-10 expression via the TLR/JAK-STAT–c-Maf axis.

During various infections, *Il10* family cytokines elicit diverse host defense mechanisms, particularly those derived from epithelial cells (*50*). *Il10* is a crucial anti-inflammatory mediator (*51*, *52*) that targets a variety of leukocytes and mainly inhibits excessive inflammatory responses. In addition, *Il10* can also promote the transformation of macrophages from M1 state to M2, exhibiting a promising effect on tissue repair (*53*–*55*). A study reported that *Il10* could promote chondrogenic differentiation and chondrocyte proliferation (*56*). *Il10*-deficient mice show a reduction in the proliferation zone of embryonic growth plates. Furthermore, *Il10* drives OPN expression in MSCs, while blocking *Il10* reduces subsequent calcification and mineralization (*53*). In this study, we found that CHG composite hydrogel–treated BMMs significantly increased the expression of CD206, a representative surface marker of M2 macrophages, and exhibited excellent osteoinductive activity both in vitro and in vivo. Thus, the CHG composite hydrogel may increase the relative expression levels of *Il10*, which, in turn, promote M2 macrophage polarization and accelerate osteogenesis.

In conclusion, we successfully fabricate zero-dimensional Arg-CDs and engineered CHG composite hydrogel that can collapse as well as intelligent controlled release of Arg-CDs in the acidic infectious bone injury microenvironment. The released Arg-CDs significantly eliminate bacteria by producing excessive ROS and promote cell proliferation by up-regulating the expression of antioxidases. Moreover, the obtained Arg-CD–based composite hydrogel up-regulates the expression of *Il10*, which fuels the osteogenesis by promoting M2 macrophage polarization. Owing to the perfect combination of excellent antibacterial activity and bone formation, our CHG composite hydrogel exhibits a highly attractive application prospect in the treatment of infectious bone repair, which notably improves the success rate of bone implants. Therefore, transformation of Arg into zero-dimensional nanomaterial endows the material with antibacterial and osteoinductive activity, which can provide inspirations for biomaterial-based tissue regeneration.

MATERIALS AND METHODS

Material preparation

Arg-CDs were synthesized following the reported method. Briefly, 500 mg of Arg was heated at 240°C for 3 hours. After cooling to room temperature, the residue was dissolved in 20 ml of ultrapure water. The Arg-CD solution was sonicated and centrifuged at 15,000 rpm for 30 min. Then, the supernatant was dialyzed against ultrapure water for 24 hours using a dialysis membrane (molecular weight cutoff = 1000 Da). Last, Arg-CDs were obtained by lyophilization.

To synthesize HA-CHO, 1.5 g of HA was dissolved in 150 ml of deionized water and then 802 mg of sodium periodate was added and stirred for 2 hours. The reaction was stopped by adding ethylene glycol (200 μl) and dialyzed against deionized water. The obtained HA-CHO was freeze-dried and stored at 4°C.

A total of 1 g of G sponge, 50 mg of photoinitiator lithium phenyl-2,4,6-trimethyl-benzoyl phosphinate, and 100 mg of HA-CHO were dissolved in 20 ml of deionized water at 37°C, after which 80 mg of Arg-CDs were added and stirred until well mixed. The CHG composite hydrogel was obtained by photocrosslinking (wavelength of 405 nm).

Material characterizations

The morphology of Arg-CDs was characterized using a transmission electron microscope (TECNAI G2 F20, FEI, USA). The diameter distribution of Arg-CDs was measured using a nanoparticle size and zeta potential analyzer (Zetasizer Nano ZS90). The molecular structure of HA-CHO and CHG composite hydrogel was detected by FTIR (Nicolet 6700, Thermo Fisher Scientific, USA). The destruction of the CHG composite hydrogel in the acidic microenvironment was performed by a mechanical test. The samples (height: 5 mm; diameter: 4.5 mm) were immersed in pH 7.2 and pH 5.5 buffer solutions at 37°C for 24 hours. Then, their compressive strength was tested (5 mm/min) using a universal force tester (Shanghai Hengyi Precision Instrument Co. Ltd., China). After freeze-drying, the structure of the CHG composite hydrogel was characterized by SEM (Quanta 250, FEI, Hillsboro, OR, USA). The properties of Arg-CDs released from the composite hydrogel were investigated by UV-vis absorption spectroscopy at different time intervals. Briefly, the composite hydrogels were immersed in pH 7.2 and pH 5.5 buffer solutions at 37°C. The release of Arg-CDs from composite hydrogels was measured at different time points. The UV-vis absorption peaks of Arg-CDs with different concentrations (125, 250, and 500 μg/ml) at a wavelength of 305 nm were measured to obtain the standard curve. According to the standard curve, the released Arg-CDs from the composite hydrogel were calculated from the results of UV-vis absorption spectroscopy.

Cell morphology and viability

BMSCs were cultured in α–minimum essential medium (Hyclone, Thermo Fisher Scientific, USA) containing 10% fetal bovine serum (Gibco) and 1% penicillin-streptomycin. BMSCs were seeded on composite hydrogels and cultured for 48 hours. Then, they were fixed with 4% paraformaldehyde for 40 min at room temperature. Afterward, the cells were washed with phosphate-buffered saline (PBS) and sealed and permeabilized with 3% bovine serum albumin solution containing 0.3% Triton X-100 for 12 hours. Then, the sample was stained with rhodamine phalloidin and 4′,6-diamidino-2-phenylindole (DAPI). Images were acquired with an inverted fluorescence microscope. For SEM scanning, BMSCs were seeded on composite hydrogels (5×10^4 cells per well) and incubated for 48 hours. Then, they were fixed with 4% paraformaldehyde for 40 min, dehydrated with gradient ethanol (10, 30, 50, 70, 85, 90, and 100%), and observed by SEM after critical point drying. Cell proliferation was evaluated by the CCK-8 assay. Briefly, BMSCs were seeded on composite hydrogels (1×10^3 cells per well). At the time points of 1, 3, and 5 days of incubation, cells

were incubated with a diluted CCK-8 agent (Dojindo, Japan) for 2 hours (CCK-8 agent:culture medium = 1:10). Then, the absorbance was measured at 450 nm of wavelength.

In vitro antibacterial properties

S. aureus was inoculated on composite hydrogels (1×10^4). The destruction performance of the composite hydrogels on biofilm was detected by AO/EB staining after 24 hours. The hydrogels were washed three times with PBS and fixed with 95% ethanol for 40 min at room temperature. Then, *S. aureus* was incubated with AO/EB reagent, and images were collected with an inverted fluorescence microscope. Next, we evaluated antibacterial properties of composite hydrogels by inhibition zone experiments. The composite hydrogels were placed on the center of an LB agar plate coated with 100 μl of *S. aureus* suspension [10^6 to 10^7 colony-forming units (CFU)/ml]. Then, the bacteria were cultured at 37°C for 18 hours. The area with no bacterial colonies was quantified to assess antibacterial activity of composite hydrogels. Antimicrobial kinetics of Arg, Arg-CDs, and composite hydrogels were performed to verify their antibacterial properties. Composite hydrogels were immersed in PBS containing *S. aureus*. The supernatant was collected at different time intervals and added to the LB agar plate to observe the colonies, which were counted using ImageJ software. The effect on bacterial biofilm formation was performed by SEM. *S. aureus* was seeded on composite hydrogels for 24 hours, which was then washed with PBS and fixed with 2.5% glutaraldehyde for 15 min. The samples were then dehydrated with gradient ethanol (10, 30, 50, 70, 85, 90, and 100%) and observed by SEM after critical point drying.

Cocultured system of cells and bacteria

The cell proliferation and antibacterial properties of composite hydrogels were evaluated. BMSCs and *S. aureus* were seeded on composite hydrogels at a ratio of 20:1 (1×10^5 cells per well, 5×10^3 CFUs per well) and incubated for 24 hours. They were washed three times with PBS and fixed with 95% ethanol for 5 min. Then, the morphologies of BMSCs and *S. aureus* were observed by SEM after dehydrating with gradient ethanol. To observe *S. aureus* that internalized and survived within BMSCs, BMSCs and *S. aureus* were labeled with DiO perchlorate (green) and DiD perchlorate (red), respectively. Then, the DiO-labeled BMSCs and DiD-labeled *S. aureus* were simultaneously seeded on hydrogels at a ratio of 20:1 (1×10^5 cells per well, 5×10^3 CFUs per well). After 24 hours, the extracellular bacteria were eliminated by gentamicin (60 μg ml^{-1}) and then fixed with 4% paraformaldehyde for 40 min. Last, the samples were stained with DAPI, and images were collected using an inverted fluorescence microscope.

Detecting ROS levels and antioxidase activities of cells and bacteria

To detect cellular and bacterial ROS levels, *S. aureus* was added to each sterile (1×10^8 CFU/ml). Next, the composite hydrogels were added to the vials and then cultured at 37°C for 30 min in a shaker. Subsequently, DCFH-DA (10 μM) was added and then incubated at 37°C for 20 min in a shaker. Last, the fluorescent intensity was measured with a fluorescence microplate reader at an excitation wavelength of 488 nm. The detection processes of ROS in BMSCs were the same as described above. Cellular and bacterial antioxidase activities, including SOD and CAT, were assessed according to the manufacturer's protocol. The effect on cellular ROS scavenging was evaluated by DCFH-DA staining. BMSCs were seeded on composite hydrogels (1×10^4 cells per well). After 24 hours, the medium was replaced with one containing 100 μM H_2O_2. BMSCs were stained with DCFH-DA agent after 24 hours of incubation, and the samples were observed using an inverted fluorescence microscope.

In vitro osteogenesis properties

BMSCs were seeded on a six-well plate (1×10^5 cells per well). After 24 hours, the medium was replaced with osteogenic differentiation medium comprising 10 mM β-glycerophosphate, 10 nM dexamethasone, and L-ascorbic acid 2-phosphate (50 μg/ml; Sigma-Aldrich, USA). The Arg, Arg-CDs, and composite hydrogels were immersed in the above osteogenic differentiation medium. After 7 days of culture, ALP staining was performed with the ALP staining kit (Beyotime, China). Alizarin red staining was executed after 21 days. The expression of typical osteogenic genes (7 days: *Alpl*, *Spp1*, and *Runx2*; 21 days: *Col1a1* and *Bglap*) and antioxidant genes (*Sirt1* and *Sod2*) was detected by real-time quantitative PCR (qPCR), while the expression of osteogenic (7 days: RUNX2 and OPN; 21 days: COL1 and OCN) and antioxidant proteins (SIRT1 and SOD2) was also measured by Western blot. As above, BMSCs were seeded on the six-well plate (1×10^5 cells per well). After 24 hours, the medium was replaced with osteogenic differentiation medium. The composite hydrogels were immersed in the above osteogenic differentiation medium and incubated with BMSCs for 7 and 21 days, respectively. Real-time qPCR analysis and Western blots were performed to detect gene transcription and protein expression levels. The primer sequences are shown in table S1.

Heterotopic ossification

The procedures were approved by the Institutional Animal Care and Use Committee of the Soochow University of China by applying Chinese national guidelines for the care and use of experimental animals (SUDA20220711A09). To measure the osteoinductivity of composite hydrogels, the cylindrical samples (diameter: 3 mm; height: 2 mm) were implanted subcutaneously on Sprague-Dawley rats (weighing 300 to 350 g). After 4 weeks, alizarin red and H&E staining were performed to observe ectopic bone formation by composite hydrogels.

In vivo infection model

An infectious lateral femoral condyle defective model was induced on Sprague-Dawley rats (weighing 300 to 350 g). After inducing anesthesia with pentobarbital sodium (30 mg/kg; Sigma-Aldrich), the hindlimbs of rats were shaved and disinfected with povidone-iodine. The femur was exposed by blunt dissection, and bone defects (diameter: 3 mm; depth: 3 mm) were formed on the femoral condyles using a bone drill. *S. aureus* (10^4 CFU/ml) were injected into the femoral condyle cavity. The composite hydrogels were implanted into the femoral condyle cavity and then irradiated with blue light (405 nm) for 30 s. The rats were euthanized 4 and 8 weeks after implantation, and the femurs were harvested and fixed with 4% paraformaldehyde for 24 hours at room temperature. Then, a micro–computed tomography scan was performed for evaluating new bone formation.

Histological analysis

Immunofluorescence, H&E, Masson, and Giemsa staining were performed for histological analysis. Rat femur specimens were decalcified in 14% EDTA for 30 days. After dehydrating with alcohol gradient, the samples were embedded in paraffin and cut into 6-μm-thick slices. All staining were performed according to the manufacturers′ protocols. The ImageJ software was used to count the viable bacteria at the site of bone defect.

mRNA library construction and sequencing

Total RNA was extracted from cells using TRIzol reagent (Invitrogen, Carlsbad, CA, USA) according to the manufacturer′s instruction. The RNA quantity was quantified using NanoDrop ND-1000 (NanoDrop, Wilmington, DE, USA). RNA integrity was assessed by Bioanalyzer 2100 (Agilent, CA, USA) with RNA integrity number (RIN) > 7.0 and confirmed by electrophoresis. RNA containing polyadenylate was purified from total RNA using Dynabeads oligo(dT)25-61005 (Thermo Fisher Scientific, CA, USA) by two rounds of purification. Then, the RNA was fragmented using the Magnesium RNA Fragmentation Module (NEB, USA) at 94°C for 5 min. cDNA was generated from cleaved RNA fragments with the SuperScript II Reverse Transcriptase (Invitrogen, USA), and a U-labeled second-stranded DNA was synthesized with *Escherichia coli* DNA polymerase I (NEB, USA), ribonuclease H (NEB, USA), and deoxyuridine triphosphate solution (Thermo Fisher Scientific, USA). An A-base was then added to the blunt ends of each strand for ligation to the indexed adapters. Each adapter contained a T-base overhang for ligating the adapter to the A-tailed fragmented DNA. The fragments were ligated to single- or dual-index adapters, and AMPureXP beads were used to perform size selection. After the heat-labile UDG enzyme (NEB, USA) treatment, ligated products were amplified from the U-labeled second-stranded DNA by PCR. The average insert size for the final cDNA library was 300 ± 50 base pairs (bp). Last, the 2 × 150-bp paired-end sequencing (PE150) was performed on an Illumina Novaseq 6000 sequencing machine (LC-Bio Technology Co. Ltd., Hangzhou, China) following the vendor′s recommended protocol.

Sequence and primary analysis

The adaptor-contaminated reads were excluded by Cutadapt software (https://cutadapt.readthedocs.io/en/stable/; version 1.9). After removing the low-quality and undetermined bases, HISAT2 software (https://daehwankimlab.github.io/hisat2/; version: 2.0.4) was used for genome mapping. The mapped reads were assembled using StringTie (http://ccb.jhu.edu/software/stringtie/; version: 1.3.4). Then, the comprehensive transcriptome was reconstructed using gffcompare software (http://ccb.jhu.edu/software/stringtie/gffcompare.shtml; version 0.9.8). Subsequently, StringTie and ballgown (www.bioconductor.org/packages/release/bioc/html/ballgown.html) were used to calculate fragments per kilobase million (FPKM) (FPKM = [total_exon_fragments/mapped_reads (millions) × exon_length (kB)]). The differentially expressed mRNAs were selected with a log (fold change) > 1.5 and $P < 0.01$ by edgeR (https://bioconductor.org/packages/release/bioc/html/edgeR.html). GO analysis was performed on Metascape (*57*). GSEA was performed using GSEA software (https://www.gsea-msigdb.org/gsea/index.jsp; version: 4.1.0) (*58*).

Measurement of *Il10* concentration

BMMs and BMSCs were seeded on composite hydrogels (1×10^5 cells per well). After 2, 4, and 6 days, the culture medium was collected separately. The concentration of *Il10* was detected using enzyme-linked immunosorbent assay kits (R&D Systems).

Characterization of macrophage polarization

BMMs were seeded on composite hydrogels (1×10^5 cells per well). After 24 hours, the medium was replaced with the conditioned media that had previously cultured BMSCs on composite hydrogels. After 3 days, CD206 and F4/80 immunofluorescence were performed, and the effect of induced macrophage polarization was detected on composite hydrogels. The immunofluorescence of CD206 at bone defect sites was also performed.

Statistical analysis

Data were presented as means ± SD. Statistical analysis (GraphPad Software, USA) was evaluated using one-way analysis of variance (ANOVA) followed by Tukey′s multiple comparison to evaluate differences between the groups. A probability value (P) less than 0.05 was considered statistically significant.

Supplementary Materials

This PDF file includes:

Figs. S1 to S15
Table S1

REFERENCES AND NOTES

1. N. Kavanagh, E. J. Ryan, A. Widaa, G. Sexton, J. Fennell, S. O′Rourke, K. C. Cahill, C. J. Kearney, F. J. O′Brien, S. W. Kerrigan, Staphylococcal osteomyelitis: Disease progression, treatment challenges, and future directions. *Clin. Microbiol. Rev.* **31**, e00084-17 (2018).
2. H. Li, S. Zhang, S. Huo, H. Tang, B. Nie, X. Qu, B. Yue, Effects of staphylococcal infection and aseptic inflammation on bone mass and biomechanical properties in a rabbit model. *J. Orthop. Translat.* **21**, 66–72 (2020).
3. L. Foulston, A. K. Elsholz, A. S. DeFrancesco, R. Losick, The extracellular matrix of Staphylococcus aureus biofilms comprises cytoplasmic proteins that associate with the cell surface in response to decreasing pH. *MBio* **5**, e01667-14 (2014).
4. S. B. Levy, B. Marshall, Antibacterial resistance worldwide: Causes, challenges and responses. *Nat. Med.* **10**, S122–S129 (2004).
5. K. Bush, P. Courvalin, G. Dantas, J. Davies, B. Eisenstein, P. Huovinen, G. A. Jacoby, R. Kishony, B. N. Kreiswirth, E. Kutter, S. A. Lerner, S. Levy, K. Lewis, O. Lomovskaya, J. H. Miller, S. Mobashery, L. J. Piddock, S. Projan, C. M. Thomas, A. Tomasz, P. M. Tulkens, T. R. Walsh, J. D. Watson, J. Witkowski, W. Witte, G. Wright, P. Yeh, H. I. Zgurskaya, Tackling antibiotic resistance. *Nat. Rev. Microbiol.* **9**, 894–896 (2011).
6. D. Wang, M. L. Kuzma, X. Tan, T. C. He, C. Dong, Z. Liu, J. Yang, Phototherapy and optical waveguides for the treatment of infection. *Adv. Drug Deliv. Rev.* **179**, 114036 (2021).
7. R. Y. Pelgrift, A. J. Friedman, Nanotechnology as a therapeutic tool to combat microbial resistance. *Adv. Drug Deliv. Rev.* **65**, 1803–1815 (2013).
8. C. T. Johnson, M. C. P. Sok, K. E. Martin, P. P. Kalelkar, J. D. Caplin, E. A. Botchwey, A. J. García, Lysostaphin and BMP-2 co-delivery reduces *S. aureus* infection and regenerates critical-sized segmental bone defects. *Sci. Adv.* **5**, eaaw1228 (2019).
9. M. Wang, Y. Yang, K. Yuan, S. Yang, T. Tang, Dual-functional hybrid quaternized chitosan/Mg/alginate dressing with antibacterial and angiogenic potential for diabetic wound healing. *J. Orthop. Translat.* **30**, 6–15 (2021).
10. Q. Wang, W. Wang, Y. Li, W. Li, L. Tan, K. Yang, Biofunctional magnesium coating of implant materials by physical vapour deposition. *Biomater. Transl.* **2**, 248–256 (2021).
11. C. Sun, J. Kang, C. Yang, J. Zheng, Y. Su, E. Dong, Y. Liu, S. Yao, C. Shi, H. Pang, J. He, L. Wang, C. Liu, J. Peng, L. Liu, Y. Jiang, D. Li, Additive manufactured polyether-ether-ketone implants for orthopaedic applications: A narrative review. *Biomater. Transl.* **3**, 116–133 (2022).
12. A. Punia, E. He, K. Lee, P. Banerjee, N. L. Yang, Cationic amphiphilic non-hemolytic polyacrylates with superior antibacterial activity. *Chem. Commun.* **50**, 7071–7074 (2014).

13. H. Xu, Z. Fang, W. Tian, Y. Wang, Q. Ye, L. Zhang, J. Cai, Green fabrication of amphiphilic quaternized β-chitin derivatives with excellent biocompatibility and antibacterial activities for wound healing. *Adv. Mater.* **30**, e1801100 (2018).
14. S. Maleki Dizaj, A. Mennati, S. Jafari, K. Khezri, K. Adibkia, Antimicrobial activity of carbon-based nanoparticles. *Adv. Pharm. Bull.* **5**, 19–23 (2015).
15. R. Wang, M. Shi, F. Xu, Y. Qiu, P. Zhang, K. Shen, Q. Zhao, J. Yu, Y. Zhang, Graphdiyne-modified TiO_2 nanofibers with osteoinductive and enhanced photocatalytic antibacterial activities to prevent implant infection. *Nat. Commun.* **11**, 4465 (2020).
16. F. Natalio, R. Andre, A. F. Hartog, B. Stoll, K. P. Jochum, R. Wever, W. Tremel, Vanadium pentoxide nanoparticles mimic vanadium haloperoxidases and thwart biofilm formation. *Nat. Nanotechnol.* **7**, 530–535 (2012).
17. L. Gao, K. M. Giglio, J. L. Nelson, H. Sondermann, A. J. Travis, Ferromagnetic nanoparticles with peroxidase-like activity enhance the cleavage of biological macromolecules for biofilm elimination. *Nanoscale* **6**, 2588–2593 (2014).
18. G. Walters, I. Pountos, P. V. Giannoudis, The cytokines and micro-environment of fracture haematoma: Current evidence. *J. Tissue Eng. Regen. Med.* **12**, e1662–e1677 (2018).
19. W. Chen, X. Shen, Y. Hu, K. Xu, Q. Ran, Y. Yu, L. Dai, Z. Yuan, L. Huang, T. Shen, K. Cai, Surface functionalization of titanium implants with chitosan-catechol conjugate for suppression of ROS-induced cells damage and improvement of osteogenesis. *Biomaterials* **114**, 82–96 (2017).
20. Y. Sun, X. Sun, X. Li, W. Li, C. Li, Y. Zhou, L. Wang, B. Dong, A versatile nanocomposite based on nanoceria for antibacterial enhancement and protection from aPDT-aggravated inflammation via modulation of macrophage polarization. *Biomaterials* **268**, 120614 (2021).
21. H. S. Kim, S. T. Nam, S. H. Mun, S. K. Lee, H. W. Kim, Y. H. Park, B. Kim, K. J. Won, H. R. Kim, Y. M. Park, H. S. Kim, M. A. Beaven, Y. M. Kim, W. S. Choi, DJ-1 controls bone homeostasis through the regulation of osteoclast differentiation. *Nat. Commun.* **8**, 1519 (2017).
22. J. Li, F. Han, J. Ma, H. Wang, J. Pan, G. Yang, H. Zhao, J. Zhao, J. Liu, Z. Liu, B. Li, Targeting endogenous hydrogen peroxide at bone defects promotes bone repair. *Adv. Funct. Mater.* **32**, 2111208 (2022).
23. M. J. Meziani, X. Dong, L. Zhu, L. P. Jones, G. E. LeCroy, F. Yang, S. Wang, P. Wang, Y. Zhao, L. Yang, R. A. Tripp, Y. P. Sun, Visible-light-activated bactericidal functions of carbon "quantum" dots. *ACS Appl. Mater. Interfaces* **8**, 10761–10766 (2016).
24. W. Bing, H. Sun, Z. Yan, J. Ren, X. Qu, Programmed bacteria death induced by carbon dots with different surface charge. *Small* **12**, 4713–4718 (2016).
25. P. Li, F. Han, W. Cao, G. Zhang, J. Li, J. Zhou, X. Gong, G. Turnbull, W. Shu, L. Xia, B. Fang, X. Xing, B. Li, Carbon quantum dots derived from lysine and arginine simultaneously scavenge bacteria and promote tissue repair. *Appl. Mater. Today* **19**, 100601 (2020).
26. J. Yang, H. Qin, Y. Chai, P. Zhang, Y. Chen, K. Yang, M. Qin, Y. Zhang, H. Xia, L. Ren, B. Yu, Molecular mechanisms of osteogenesis and antibacterial activity of Cu-bearing Ti alloy in a bone defect model with infection in vivo. *J. Orthop. Translat.* **27**, 77–89 (2021).
27. D. J. Dwyer, P. A. Belenky, J. H. Yang, I. C. MacDonald, J. D. Martell, N. Takahashi, C. T. Chan, M. A. Lobritz, D. Braff, E. G. Schwarz, J. D. Ye, M. Pati, M. Vercruysse, P. S. Ralifo, K. R. Allison, A. S. Khalil, A. Y. Ting, G. C. Walker, J. J. Collins, Antibiotics induce redox-related physiological alterations as part of their lethality. *Proc. Natl. Acad. Sci. U.S.A.* **111**, E2100–E2109 (2014).
28. H. L. Su, C. C. Chou, D. J. Hung, S. H. Lin, I. C. Pao, J. H. Lin, F. L. Huang, R. X. Dong, J. J. Lin, The disruption of bacterial membrane integrity through ROS generation induced by nanohybrids of silver and clay. *Biomaterials* **30**, 5979–5987 (2009).
29. W. Jiang, M. Zhou, Z. Cong, J. Xie, W. Zhang, S. Chen, J. Zou, Z. Ji, N. Shao, X. Chen, M. Li, R. Liu, Short guanidinium-functionalized poly(2-oxazoline)s displaying potent therapeutic efficacy on drug-resistant fungal infections. *Angew. Chem. Int. Ed. Engl.* **61**, e202200778 (2022).
30. Y. Cao, J. Gu, S. Wang, Z. Zhang, H. Yu, J. Li, S. Chen, Guanidine-functionalized cotton fabrics for achieving permanent antibacterial activity without compromising their physicochemical properties and cytocompatibility. *Cellulose* **27**, 6027–6036 (2020).
31. S. Guo, Q. Huang, Y. Chen, J. Wei, J. Zheng, L. Wang, Y. Wang, R. Wang, Synthesis and bioactivity of guanidinium-functionalized pillar[5]arene as a biofilm disruptor. *Angew. Chem. Int. Ed. Engl.* **60**, 618–623 (2021).
32. Y. Zhou, G. Liu, H. Huang, J. Wu, Advances and impact of arginine-based materials in wound healing. *J. Mater. Chem. B* **9**, 6738–6750 (2021).
33. H. J. Jian, R. S. Wu, T. Y. Lin, Y. J. Li, H. J. Lin, S. G. Harroun, J. Y. Lai, C. C. Huang, Super-cationic carbon quantum dots synthesized from spermidine as an eye drop formulation for topical treatment of bacterial keratitis. *ACS Nano* **11**, 6703–6716 (2017).
34. B. Shtaif, M. Bar-Maisels, Y. Gabet, S. Hiram-Bab, M. Yackobovitch-Gavan, M. Phillip, G. Gat-Yablonski, Cartilage-specific knockout of Sirt1 significantly reduces bone quality and catch-up growth efficiency. *Bone* **138**, 115468 (2020).
35. Q. Chen, J. Li, F. Han, Q. Meng, H. Wang, Q. Wei, Z. Li, F. Li, E. Xie, X. Qin, S. Chen, W. Wang, C. Liu, B. Li, F. Han, A multifunctional composite hydrogel that rescues the ROS microenvironment and guides the immune response for repair of osteoporotic bone defects. *Adv. Funct. Mater.* **32**, 2201067 (2022).
36. Z. Wang, Z. Wang, W. Huang, J. Suo, X. Chen, K. Ding, Q. Sun, H. Zhang, Antioxidant and anti-inflammatory activities of an anti-diabetic polysaccharide extracted from Gynostemma pentaphyllum herb. *Int. J. Biol. Macromol.* **145**, 484–491 (2020).
37. K. V. Hatware, S. Sharma, K. Patil, M. Shete, S. Karri, G. Gupta, Evidence for gastroprotective, anti-inflammatory and antioxidant potential of methanolic extract of Cordia dichotoma leaves on indomethacin and stress induced gastric lesions in Wistar rats. *Biomed. Pharmacother.* **103**, 317–325 (2018).
38. Z. Xu, G. Liu, P. Liu, Y. Hu, Y. Chen, Y. Fang, G. Sun, H. Huang, J. Wu, Hyaluronic acid-based glucose-responsive antioxidant hydrogel platform for enhanced diabetic wound repair. *Acta Biomater.* **147**, 147–157 (2022).
39. N. L. Vanden Braber, I. Novotny Nunez, L. Bohl, C. Porporatto, F. N. Nazar, M. A. Montenegro, S. G. Correa, Soy genistein administered in soluble chitosan microcapsules maintains antioxidant activity and limits intestinal inflammation. *J. Nutr. Biochem.* **62**, 50–58 (2018).
40. Y. Wang, C. Luan, G. Zhang, C. Sun, The transcription factor cMaf is targeted by mTOR, and regulates the inflammatory response via the TLR_4 signaling pathway. *Int. J. Mol. Med.* **41**, 2935–2942 (2018).
41. C. Imbratta, H. Hussein, F. Andris, G. Verdeil, c-MAF, a Swiss Army knife for tolerance in lymphocytes. *Front. Immunol.* **11**, 206 (2020).
42. J. Xu, Y. Yang, G. Qiu, G. Lal, Z. Wu, D. E. Levy, J. C. Ochando, J. S. Bromberg, Y. Ding, c-Maf regulates IL-10 expression during Th17 polarization. *J. Immunol.* **182**, 6226–6236 (2009).
43. S. Ruberti, E. Bianchi, P. Guglielmelli, S. Rontauroli, G. Barbieri, L. Tavernari, T. Fanelli, R. Norfo, V. Pennucci, G. C. Fattori, C. Mannarelli, N. Bartalucci, B. Mora, L. Elli, M. A. Avanzini, C. Rossi, S. Salmoiraghi, R. Zini, S. Salati, Z. Prudente, V. Rosti, F. Passamonti, A. Rambaldi, S. Ferrari, E. Tagliafico, A. M. Vannucchi, R. Manfredini, Involvement of MAF/SPP1 axis in the development of bone marrow fibrosis in PMF patients. *Leukemia* **32**, 438–449 (2018).
44. Y. W. Qiang, S. Ye, Y. Chen, A. F. Buros, R. Edmonson, F. van Rhee, B. Barlogie, J. Epstein, G. J. Morgan, F. E. Davies, MAF protein mediates innate resistance to proteasome inhibition therapy in multiple myeloma. *Blood* **128**, 2919–2930 (2016).
45. J. Kienast, W. E. Berdel, c-maf in multiple myeloma: An oncogene enhancing tumor-stroma interactions. *Cancer Cell* **5**, 109–110 (2004).
46. K. Kataoka, Multiple mechanisms and functions of maf transcription factors in the regulation of tissue-specific genes. *J. Biochem.* **141**, 775–781 (2007).
47. V. Lopez-Pajares, K. Qu, J. Zhang, D. E. Webster, B. C. Barajas, Z. Siprashvili, B. J. Zarnegar, L. D. Boxer, E. J. Rios, S. Tao, M. Kretz, P. A. Khavari, A LncRNA-MAF:MAFB transcription factor network regulates epidermal differentiation. *Dev. Cell* **32**, 693–706 (2015).
48. K. Nishikawa, T. Nakashima, S. Takeda, M. Isogai, M. Hamada, A. Kimura, T. Kodama, A. Yamaguchi, M. J. Owen, S. Takahashi, H. Takayanagi, Maf promotes osteoblast differentiation in mice by mediating the age-related switch in mesenchymal cell differentiation. *J. Clin. Invest.* **120**, 3455–3465 (2010).
49. E. L. Soucie, Z. Weng, L. Geirsdottir, K. Molawi, J. Maurizio, R. Fenouil, N. Mossadegh-Keller, G. Gimenez, L. VanHille, M. Beniazza, J. Favret, C. Berruyer, P. Perrin, N. Hacohen, J. C. Andrau, P. Ferrier, P. Dubreuil, A. Sidow, M. H. Sieweke, Lineage-specific enhancers activate self-renewal genes in macrophages and embryonic stem cells. *Science* **351**, eaad5510 (2016).
50. W. Ouyang, S. Rutz, N. K. Crellin, P. A. Valdez, S. G. Hymowitz, Regulation and functions of the IL-10 family of cytokines in inflammation and disease. *Annu. Rev. Immunol.* **29**, 71–109 (2011).
51. M. Saraiva, P. Vieira, A. O'Garra, Biology and therapeutic potential of interleukin-10. *J. Exp. Med.* **217**, e20190418 (2020).
52. T. H. Kim, K. Yang, M. Kim, H. S. Kim, J. L. Kang, Apoptosis inhibitor of macrophage (AIM) contributes to IL-10-induced anti-inflammatory response through inhibition of inflammasome activation. *Cell Death Dis.* **12**, 19 (2021).
53. O. R. Mahon, D. C. Browe, T. Gonzalez-Fernandez, P. Pitacco, I. T. Whelan, S. Von Euw, C. Hobbs, V. Nicolosi, K. T. Cunningham, K. H. G. Mills, D. J. Kelly, A. Dunne, Nano-particle mediated M2 macrophage polarization enhances bone formation and MSC osteogenesis in an IL-10 dependent manner. *Biomaterials* **239**, 119833 (2020).
54. S. Chen, H. Wang, Y. Su, J. V. John, A. McCarthy, S. L. Wong, J. Xie, Mesenchymal stem cell-laden, personalized 3D scaffolds with controlled structure and fiber alignment promote diabetic wound healing. *Acta Biomater.* **108**, 153–167 (2020).
55. S. Tan, Y. Wang, Y. Du, Y. Xiao, S. Zhang, Injectable bone cement with magnesium-containing microspheres enhances osteogenesis via anti-inflammatory immunoregulation. *Bioact. Mater.* **6**, 3411–3423 (2021).
56. Y. K. Jung, G. W. Kim, H. R. Park, E. J. Lee, J. Y. Choi, F. Beier, S. W. Han, Role of interleukin-10 in endochondral bone formation in mice: Anabolic effect via the bone morphogenetic protein/Smad pathway. *Arthritis Rheumatol.* **65**, 3153–3164 (2013).

57. Y. Zhou, B. Zhou, L. Pache, M. Chang, A. H. Khodabakhshi, O. Tanaseichuk, C. Benner, S. K. Chanda, Metascape provides a biologist-oriented resource for the analysis of systems-level datasets. *Nat. Commun.* **10**, 1523 (2019).
58. A. Subramanian, P. Tamayo, V. K. Mootha, S. Mukherjee, B. L. Ebert, M. A. Gillette, A. Paulovich, S. L. Pomeroy, T. R. Golub, E. S. Lander, J. P. Mesirov, Gene set enrichment analysis: A knowledge-based approach for interpreting genome-wide expression profiles. *Proc. Natl. Acad. Sci. U.S.A.* **102**, 15545–15550 (2005).

Acknowledgments
Funding: We are grateful for the funding support from the National Natural Science Foundation of China (81925027, 31872748, and 82111530157), Postgraduate Research & Practice Innovation Program of Jiangsu Province (KYCX22_3232), the Priority Academic Program Development (PAPD) of Jiangsu Higher Education Institutions, and the Key Laboratory of Orthopaedics of Suzhou (SZS2022017). **Author contributions:** J.L., J.M., H.S., X.X., F.H., and B.L. designed the research. J.L., J.M., H.S., M.Y., H.W., Q.M., Z.L., D.L., J.B., and G.L. performed the experiments. J.L., J.M., and H.S. analyzed the data. J.L., J.M., H.S., X.X., F.H., and B.L. wrote the paper. **Competing interests:** The authors declare that they have no competing interests. **Data and materials availability:** All data needed to evaluate the conclusions in the paper are present in the paper and/or the Supplementary Materials.

Submitted 19 November 2022
Accepted 20 April 2023
Published 26 May 2023
10.1126/sciadv.adf8645